Quantifying the Uncertainty Imposed by Inaccurate Modeling of Active Distribution Grids

Johanna Vorwerk*†, Uros Markovic*, Petros Aristidou‡, and Gabriela Hug*
*Power Systems Laboratory, ETH Zürich, Zürich, Switzerland
‡Sustainable Power Systems Laboratory, Cyprus University of Technology, Limassol, Cyprus
†vorwerkj@ethz.ch

***Abstract*—Replacing conventional generation with inverter-interfaced units has turned distribution networks (DNs) from consumers to active and responding intelligent DNs. These modern DNs contain several devices that can support the transmission network (TN) and system stability. Typically, deterministic and aggregated models for inverter-interfaced generation and conventional loads are used to include entire DNs in bulk system stability studies, and contributions from smart loads are neglected. This approach introduces errors to the dynamic modeling that can lead to instabilities. In this paper, we first present a full detailed model of a modern DN, enhancing existing thermal load and distributed generation models to include frequency and voltage support and protection functions required in low-inertia systems. Then, we incorporate the uncertainty that stems from the parameterization of such units using a Monte-Carlo method. Finally, we assess the impact of neglecting specific protection and support functions against frequency disturbances. The results show the crucial importance of accurately modeling protection and support functions to analyze the impact of modern DNs on bulk system stability. In addition, the findings highlight the increased relevance of considering uncertainty in stability studies of weak and low-inertia power systems.**

***Index Terms*—Active distribution network, inverter-based generator, demand side resources, frequency stability, low-inertia systems, Monte Carlo simulations**

I. Introduction

Modern power systems face an increasing penetration of inverter based generation (IBG). Besides the rising share of decentralized renewable generation units, such as wind and PV plants, power system loads are increasingly connected via power electronic equipment. In the last decade, several solutions such as grid-forming and grid-following control of IBG or fast demand response strategies have been suggested in the literature to cope with the resulting decline in system inertia and damping [1].

For most proposed schemes, the stability analysis is performed using a linear framework and applied only to the transmission network (TN) level. While [2] uses detailed differential-algebraic equation (DAE) models to investigate the stability of low inertia TNs under changing levels of VSC penetration, they neglect resources in the subordinated distribution networks (DNs). The work in [3] expands this approach and derives an aggregate DAE model for virtual power plants to be used in TN frequency studies. However, these models are deterministic and neglect the operational limits and the impact of smart loads.

DN limits are included in the control design in [4]. Besides developing a centralized, coordinated control scheme for DNs, the authors consider the flexibility regions provided by different IBG types. Nevertheless, the applied models neither reflect the underlying uncertainty of the initial operating conditions nor the uncertainty associated with the model parameterization or the operating limits of the distributed devices.

Parametric uncertainty of DAE models and the vagueness of the initial operating point are studied in [5, 6]. In [5] a Monte-Carlo (MC) analysis to reflect parametric uncertainty is performed, and [6] uses the previous findings to tune dynamic DN equivalents suitable for large-disturbance TN studies. While the applied models consider individual units' protection and security limits, they neglect internal DN limits and fast states in the inverter controls. Furthermore, demand-side management contribution (see e.g. [7,8]) is ignored. Moreover, in all cases the considered faults are voltage dips, while frequency disturbances are not considered.

Inspired by the approach in [6], this work proposes a method to quantify the parametric uncertainty of distributed units in frequency stability studies. As such, MC analysis is performed on a detailed deterministic DAE model of a DN that incorporates different details of unit protections, limits, and demand-side resources. The contributions are three-fold:

- First, we provide an active thermal load model (ATL) that includes unit protections, support functions and operational limits as required in modern grid codes. At the same time, we enhance the IBG model from [6] to respond to frequency disturbances.
- Second, frequency disturbances are applied to analyze the effect of the DN model and parametric uncertainty on the power exchanged at the TN connection point. To this end, MC simulations are performed for two TN disturbances and different unit protection configurations. For the latter, device protection and support functions are switched on or off to study the effect of protection and support modeling.
- Finally, we study how the different levels of modeling details influence the results for TN frequency stability metrics such as the maximum frequency deviation and rate of change of frequency (ROCOF). Results indicate that accurate representation of protection and support functions of all active DN devices, including loads, is essential for assessing stability, especially for weak TNs.

The remainder of the paper is structured as follows: Section II formulates the deterministic models for each of the DN components and the TN equivalent used in this study. Then, Section III outlines the MC simulation approach to assess parametric uncertainty and gives an overview of the variable parameters. Section IV introduces, evaluates and discusses the performed MC case studies and Section V concludes the paper.

II. Deterministic Modeling of Grid Components

While standard models are applied for lines, transformers, induction motors, and synchronous machines, recently developed representations for IBGs and ATLs that employ modern protection and grid support options are adapted to comply with modern grid codes, e.g. [9–11].

Phasor approximation is assumed to hold for our study, and therefore algebraic equations are used to describe the network. Including line dynamics would significantly increase the computational burden. At the same time, their effect on the uncertainty

of the power exchange at the TN/DN interface should likely be investigated but this is not the aim of the presented work.

In the following, all loads and distributed generators are modeled as current injections. The bus voltage components (v_x, v_y) resulting from the power flow are treated as inputs to each component, whereas the current components (i_x, i_y) are the outputs of the individual units. ATL and IBG devices transform the stationary reference of the grid (xy) to a rotational reference frame (pq) to enable decoupled control of active and reactive power. A corresponding subscript marks the variables. Note that vectors $\boldsymbol{x}$ and matrices $\boldsymbol{X}$ are indicated by bold symbols, while phasors are highlighted by $\underline{\boldsymbol{x}}$. Scalars in capital letters represent a quantity in physical units. Otherwise, they are based on the per-unit system. Furthermore, $x^\star$ represents an external setpoint of a model, while $\overline{x}$ stands for an internally computed reference.

A. Distribution Grid

The DN is modeled with the following algebraic system of equations:

$$\underline{\boldsymbol{i}} = \boldsymbol{Y}\,\underline{\boldsymbol{v}}, \tag{1}$$

where $\underline{\boldsymbol{i}}$ is the vector of complex current injections, $\underline{\boldsymbol{v}}$ represents the nodal voltage phasors and $\boldsymbol{Y}$ the admittance matrix, correspondingly. $\boldsymbol{Y}$ includes the line and transformer impedances at fundamental, hence nominal frequency f_n. All lines and the transformer connecting the DN to the transmission level are modeled with standard Π-equivalents as introduced in [12].

B. Background Load

Each node in the DN can connect different loads and generation. While ATLs and IBGs are considered individually, all other load components are summarized by a generalized background load. The load power S consists of a static and a dynamic part $S = P + jQ = (P_l + P_{\mathrm{im}}) + j(Q_l + P_{\mathrm{im}})$ where P_l, Q_l represent the active and reactive power of the static load component, P_{im}, Q_{im} depict the dynamic load consumption, respectively.

1) Static component: An exponential model as introduced in [12] is used for the static part. The reactive and active power are described by:

$$P_l = (1 - f_{\mathrm{im}})P_0 \left(\frac{V}{V_0}\right)^{\alpha}, \quad Q_l = (Q_0 - Q_{\mathrm{im},0}) \left(\frac{V}{V_0}\right)^{\beta}, \tag{2}$$

where P_0 and Q_0 are the initial power consumption of the background load at a particular node, f_{im} is the fraction initially consumed by dynamic loads, $Q_{\mathrm{im},0}$ is the initial reactive power consumption of the dynamic part and V_0 is the initial voltage at the load bus. The load exponents α, β adjust the influence of the voltage magnitude V on the power consumption.

2) Dynamic component: The dynamic part of the load model represents a single cage induction machine (IM) with a third-order model, taken from [6, 12]. The initial active ($P_{\mathrm{im},0}$) and reactive power ($Q_{\mathrm{im},0}$) consumed by the IM are described by:

$$P_{\mathrm{im},0} = f_{\mathrm{im}} P_0, \qquad Q_{\mathrm{im},0} = P_{\mathrm{im},0} \tan(\varphi_{\mathrm{im}}), \tag{3}$$

where $\varphi_{\mathrm{im}} = \cos^{-1}(\cos(\varphi_{\mathrm{im}}))$, and $\cos(\varphi_{\mathrm{im}})$ is the power factor of the IM. The nominal power S_n is determined by the load factor LF with $S_n = P_{\mathrm{im},0}\,(\mathrm{LF})^{-1}$. A detailed formulation of the IM third-order model, in particular the stator, rotor and flux-current relations can be found in [6, 12].

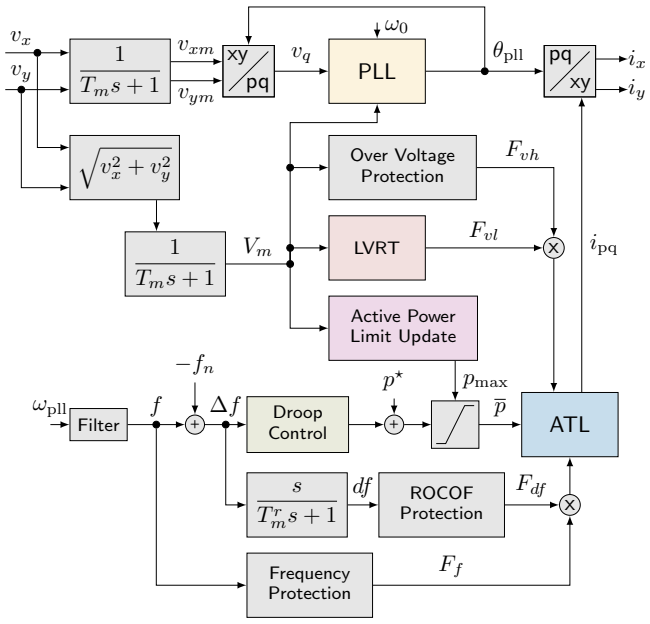

Fig. 1. Overview of the deterministic continuous thermal load model.

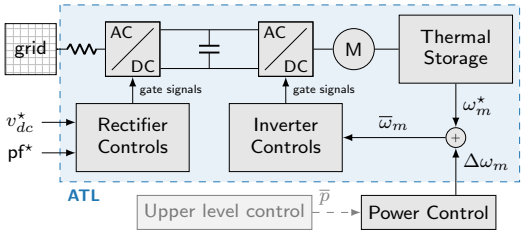

Fig. 2. Block diagram of the inner general thermal load model. It corresponds to the ATL block in Fig. 1.

C. Active Thermal Loads

The ATL model captures the primary behavior of thermal loads, i.e. heat pumps, refrigeration, and air conditioning devices, while ignoring fast switching of the internal power electronics. Fig. 1 provides an overview of the implemented model. Besides incorporating the latest grid supporting and protection functions such as Low Voltage Ride Through (LVRT), droop control, and ROCOF protection, the inherent dynamics of the thermal load, such as the inner motor, inverter, and rectifier control loops, are included in detail. While the thermal load model was enhanced from [13], the protection and support functions are added to comply with the requirements for energy consumers in [11]. Although [11] allows the units to reconnect when specific conditions are met, this function is not implemented because the required time constants exceed the time scales that are considered in this work.

1) Inner ATL Model: The applied thermal load model, represented by the blue block in Fig. 1, is suitable for various thermal devices based on variable speed technology. In particular, it is valid for heat pumps, refrigeration, and air conditioning devices based on brushless DC motors, induction machines, or permanent magnet synchronous machines. Fig. 2 provides a block diagram of the implementation. For a detailed mathematical formulation, the reader is referred to [8].

In general, the thermal device connects to the grid via a sequence of a rectifier, a DC link, an inverter, and a motor, as indicated in Fig. 2. While the rectifier PI-controls maintain the DC link voltage v_{dc} and the power factor pf at the terminal

through decoupled current control, the rotational speed control manages the thermal storage temperature by adjusting the motor speed ω_m. The inverter controls consist of a sequence of motor speed and current PI controls. Without grid support, the reference motor speed $\overline{\omega}_m$ is solely determined by the temperature control. Note that the temperature control is not implemented. Hence the required rotational speed $\omega_m^\star$ to maintain a constant temperature is treated as an external setpoint in the model. When the supervisory level requests a change in active power, it is achieved by manipulating the rotational speed reference through the external power control loop that outputs the required change in speed $\Delta\omega_m$.

While the model is taken from [13], the following changes apply: For computational reasons the compressor in the thermal unit is assumed to draw constant torque. As stated in [8], such an assumption is appropriate for a range of thermal devices. Furthermore, limiters on the active power and rotational speed are introduced to ensure realistic operating conditions.

2) Phase Locked Loop: The Phase-Locked Loop (PLL) aligns the unit's rotating reference frame (pq) to the voltage at the point of coupling by estimating the voltage angle θ. The ATL's p-axis is aligned with the voltage phasor in steady-state, and the q-axis component is zero. The reference frame rotates with the PLL estimate of the grid frequency ω_{pll}, which equals the grid frequency in steady-state and provides the alignment angle θ_{pll}. The transformation between the reference frames follows:

$$x_p = x_x \cos\theta_{\text{pll}} + x_y \sin\theta_{\text{pll}}, \tag{4a}$$
$$x_q = -x_x \sin\theta_{\text{pll}} + x_y \cos\theta_{\text{pll}}, \tag{4b}$$

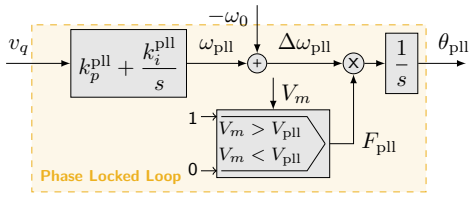

Fig. 3. Block diagram of the PLL with low voltage lock in. It corresponds to the yellow block in Fig. 1.

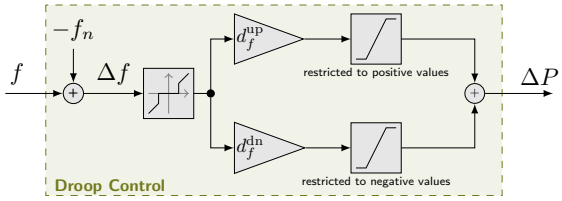

Fig. 4. Block diagram of the droop control including a deadband and asymmetric droop constants. It corresponds to the green block in Fig. 1.

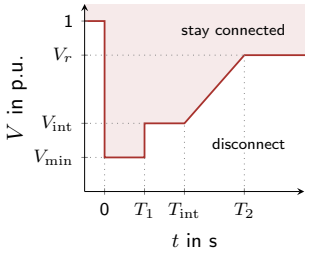

Fig. 5. Implementation of the LVRT curve for ATLs and VSCs. It corresponds to the red block in Fig. 1.

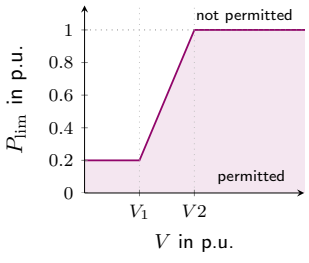

Fig. 6. Implementation of the acitve power limit for ATLs during under-voltages. It corresponds to the purple block in Fig. 1.

where x represents the current and voltage components.

A representative block diagram of the implemented PLL is depicted in Fig. 3. In low voltage conditions, i.e. when the voltage drops below a threshold V_{pll}, the PLL angle is temporarily frozen via the PLL flag F_{pll} to emulate the real behavior of PLLs.

3) Frequency Protection: As soon as the frequency is outside of the predefined operating range, the unit is tripped by activating the frequency flag F_f with:

$$F_f = \begin{cases} 0 & f < f_{\min} \text{ or } f > f_{\max} \\ 1 & f_{\min} \le f \le f_{\max} \end{cases}. \tag{5}$$

The frequency protection limit is implemented asynchronously, i.e. the deviation of the lower frequency limit $f_{\min}$ and the upper limit $f_{\max}$ from the nominal frequency deviate.

4) Frequency Droop: When the frequency stays within the acceptable limits, the device is capable of supplying a fast power reserve by employing the frequency droop technique displayed in Fig. 4. As soon as the frequency deviation Δf exceeds a deadband limit, the power reference of the unit is adapted by Δp. Similar to the WECC models for wind turbines and battery systems [14, 15], the implementation permits asynchronous droop gains for over-frequency (d_f^{up}) and under-frequency (d_f^{dn}) events. Note that the frequency f is obtained by filtering the PLL-estimate ω_{pll} as shown in Fig. 1.

5) ROCOF Protection: As indicated in Fig. 1, the ROCOF df is obtained by passing the frequency mismatch Δf through a first order derivative block with the measurement time constant T_m^r. As soon as a ROCOF threshold $df_{\max}$ is exceeded the unit trips by activating the ROCOF flag F_{df} with:

$$F_{df} = \begin{cases} 0 & |df| < df_{\max} \\ 1 & |df| \ge df_{\max} \end{cases}. \tag{6}$$

Hence, the implemented limits are symmetric.

6) Over-voltage Protection: When the measured voltage V_m exceeds a threshold $V_{\max}$ the unit is tripped without delay. To switch the unit off, the over-voltage flag F_{vh} is set to zero once the voltage magnitude threshold of $V_{\max}$ is exceeded:

$$F_{vh} = \begin{cases} 0 & V_m < V_{\max} \\ 1 & V_m \ge V_{\max} \end{cases}. \tag{7}$$

7) Low-Voltage Ride Through: Similar to distributed generation and battery devices, the ATL remains in service for the under-voltage conditions defined by the Low-Voltage Ride Through (LVRT) curve in Fig. 5. As soon as the measured voltage V_m reaches the disconnection zone, the unit trips without delay by activating the LVRT flag F_{vl}.

8) Active Power Limiter: For energy-consuming devices, [11] requires a reduction of the maximum active power consumption during under-voltage events to support the voltage. Fig. 6 provides an overview of the permitted power demand. The active power demand limit is reduced gradually once the voltage is lower than V_2, i.e. any operation point in the shaded area is permitted. If the unit did not operate at its nominal power before the under-voltage event, the consumption may remain constant as long as it stays within the permitted range.

D. Distributed Generation

Similar to the ATL model, the IBG representation captures the primary dynamics of distributed generation units. It is advanced from [6] and showcased in Fig. 7. In particular, the frequency control in [6] has been replaced with standard droop control

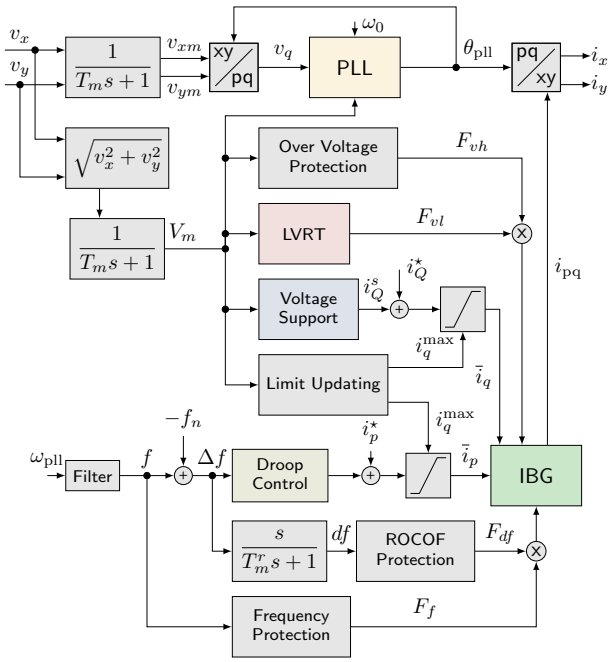

Fig. 7. Overview of the deterministic distributed generation model.

as suggested in [15]. Furthermore, ROCOF measurement and protection are added. Since most of the protection and support functions are identical to the ones implemented for the ATL, only the ones that deviate are described in the following.

1) Inner IBG Model: Unlike the ATL model, the IBG model only considers the outer loop dynamics of its controllers, assuming good tracking performance of the current control and neglecting the internal fast dynamics [6]. The green IBG block in Fig. 7 determines the inverter current i_{pq} through:

$$i_x = (T_g s + 1)^{-1}\, \bar{i}_x, \tag{8}$$

where T_g is the current control time constant, and the subscript x stands for the pq current components, respectively. The active current reference $\bar{i}_p$ is computed from the active power reference $\overline{p}$ with $\bar{i}_p = \overline{p}/V_m$. The reactive current reference is assumed to be an external setpoint. While the reactive current may change instantaneously, a limiter restricts the rate of change of active current to meet the requirements in [9–11].

2) Low-Voltage Ride Through: The same LVRT curve as in Fig. 5 applies. However, to comply with [9–11] the units reconnect after a predefined time as long as no protection flag is activated. This feature is not implemented for the thermal loads, as they require downtimes that are longer than the simulation time range considered in this work. At the same time, demand response schemes with switching of thermal loads usually employ complex reconnection procedures to prevent uniformity within an aggregation and meet compressor lockout constraints [11, 16].

3) Voltage Support: In correspondence with [9–11], the units are able to support the terminal voltage by providing additional reactive current i_q^s. The required reactive current injection depends on the measured voltage and follows

$$i_q^s = \begin{cases} k_1\,(V_{s1} - V_m) + m i_n & V_m \le V_{s1} \\ 0 & V_{s1} < V_m \le V_{s2} \\ k_2\,(V_{s2} - V_m) - n i_n & V_m > V_{s2} \end{cases} \tag{9}$$

TABLE I
VARIATION OF PARAMETERS.

Active Thermal Load		**Induction Machines**	
PLL time constant τ_{pll}	$[0.05, 0.1]$ s	Stator resistance r_s	$[0.03, 0.13]$ p.u.
Power control time constant τ_p	$[0.01, 0.03]$ s	Rotor resistance r_r	$[0.03, 0.13$ p.u.
Inertia constant H	$[0.03, 0.5]$ s	Magnetizing inductance l_m	$[2.5, 4]$ p.u.
Friction constant b	$[0.0005, 0.002]$ p.u.	Stator inductance l_s	$[0.07, 0.15]$ p.u.
Input resistance r_t	$[0.005.0.05]$ p.u.	Rotor inductance l_r	$[0.06, 0.15]$ p.u.
Input impedance l_t	$[0.1, 0.9]$ p.u.	Inertia constant H	$[0.2, 1]$ s
Anchor resistance r_a	$[0.01, 0.1]$ p.u.	Load factor LF	$[0.4, 0.6]$
		Power factor $\cos\varphi$	$[0.85, 0.95]$
IBG Units		**Static Loads**	
PLL time constant τ_{pll}	$[0.05, 0.1]$ s	Load exponent α	$[1, 2]$
Current control time constant τ_i	$[0.01, 0.03]$ s	Load exponent β	$[1.5, 3]$
Current ramp limit $\frac{di_p}{dt}$	$[0.2, 0.5]\,\frac{\text{p.u.}}{s}$	Initial consumption 1-f_{Pm}	$[0.8, 1]$

where the parameters m, n, k_1, k_2, V_{s1}, V_{s2} allow to change the characteristic, or turn it off and i_n is the nominal inverter current.

4) Limit Updating: In compliance with [6, 11] the IBG prioritizes reactive power injections during under-voltages. Thus, the active and reactive current limits are given by:

$$i_p^{\max} = P_{\text{flag}} i_n + (1 - P_{\text{flag}})\sqrt{i_n^2 - i_q^2}, \tag{10a}$$

$$i_q^{\max} = P_{\text{flag}} \sqrt{i_n^2 - i_p^2} + (1 - P_{\text{flag}}) i_n, \tag{10b}$$

where the binary P_{flag} allows to switch between active and reactive current priority. As long as no voltage support is required, it is set to one and prioritizes active power injection. During abnormal voltage conditions, i.e. V_m is outside of (V_{s1}, V_{s2}), P_{flag} is zero and ensures reactive current priority to support the voltage.

E. Transmission Grid Equivalent

Considering that the transmission grid equivalent needs to capture frequency dynamics and control, an equivalent synchronous machine (SM) represents the TN. The SM is represented with a fifth-order model [12] and connected to the TN/DN-interface via an additional line. The parameters for the SM and line are chosen to meet the short circuit power and R/X-ratio of the TN. A first-order governor is implemented by using the standard IEEE TGOV1 model from [17], with $T_2 = T_3 = 0$. The minimum and maximum voltages are set to $V_{\min} = 0$ p.u. and $V_{\max} = 1$ p.u., respectively.

III. ASSESSING PARAMETRIC UNCERTAINTY

One of the primary aims of this work is to analyze the uncertainty imposed on the DN/TN power exchange by the inaccurate knowledge and modelling of the DN components. The aforementioned dynamic models contain parameters that are not known accurately. This statement especially holds for power system loads since they are usually considered with aggregated models and typical parameters. Even grid codes for distributed generation allow for some degree of freedom for equipment parameterization and specify boundary conditions only [6, 9, 10]. Thus, after identifying the parameters that introduce uncertainty from the perspective of a grid operator, a simulation-based randomized MC approach is used to quantify the impact of parametric uncertainty.

Similar to the assumptions in [5,6], the considered uncertainty stems from the unit's parameters and load distribution of the background loads, i.e. dynamic and static background load components. The initial operating condition of the DN is assumed to be known. Furthermore, the grid model itself is assumed accurate.

All uncertain parameters and their respective ranges are listed in Tab. I. For the induction machines, static load model and IBG units, the typical parameters mentioned in [6] are used. Not all

parameters of the ATL are included as uncertain parameters. In addition to all physical motor parameters, i.e. the motor inertia H, friction constant b, and anchor resistance r_a, only the outer control loop parameters are included due to the inner control loop being significantly faster. Nonetheless, the speed control PI-parameters $k_{p\omega}$, $k_{i\omega}^i$ are adapted according to the inertia of the machine with

$$k_{p\omega}^i = 2H^i\omega_{sc}, \qquad k_{i\omega}^i = k_p^\omega\omega_{sc}/5, \tag{11}$$

where ω_{sc} is the constant control bandwidth, and the superscript i is the index of the MC simulation. The adjustment is essential to ensure stable operation of the individual units.

For each MC simulation, the parameters are drawn from the ranges in Tab. I. Since the statistical distribution of the parameters is unknown, a uniform distribution as suggested in [18] is considered. For each unit in the grid, one set of parameters per MC simulation is drawn, i.e. the PLL time constants for all devices differ during one simulation and from one simulation to the next.

IV. Case Studies

The case studies are performed on the CIGRE European 18 bus residential low voltage network published in [19] and displayed in Fig. 8. First, the modifications of the test system are discussed. Then, the model implementation and an overview of the test cases are followed by the presentation of the results.

A. Test System

While all line, transformer, and grid equivalent parameters are taken from [19], the load parameters are modified to accommodate the additional distributed units. In particular, the initial loads are reduced to 50% to ensure that voltages stay within the bounds of 0.9 p.u. to 1.1 p.u. Then, a share of the reduced load is considered as a thermal load. According to German data, the share of thermal load in residential grids varies from 19% to 42% [20]. The active thermal load shares in the test case vary from 7% to 25% to accommodate the fact that probably not all units can supply reserve simultaneously. The initial operating conditions for the ATLs and IBGs are stated in Fig. 8 next to the buses. Note that all ATL and IBG units consume or generate active power only, i.e. they operate at a power factor of one. The protection and support settings comply with [11], and are taken from [6] whenever the primary resource did not provide values. The key parameters are listed in Tab. II.

B. Model Implementation

The test case and all models are implemented in RAMSES. Details are provided in [21]. All support and protection functions are included such that they can be switched on or off. The ATL model was validated against an existing implementation in Matlab that was used in previous work [13].

C. Test Cases

Time-domain MC case studies are conducted for two different TN conditions. The first set considers the TN as a strong grid with a short-circuit power of $S_{sc} = 150$ MVA and $6s$ of inertia. Considering data for weak TN grids in Cyprus, the short circuit power is reduced to $S_{sc} = 75$ MVA for the second case, and inertia is reduced to 1.5s. In both scenarios, the nominal power of the SM representing the TN equals the nominal power of the transformer connecting the DN. Thus, uncertainty in the DN can be reflected in TN quantities like the system's frequency. It is similar to assuming that the TN connects several DNs in parallel that all respond to a TN disturbance in the same fashion.

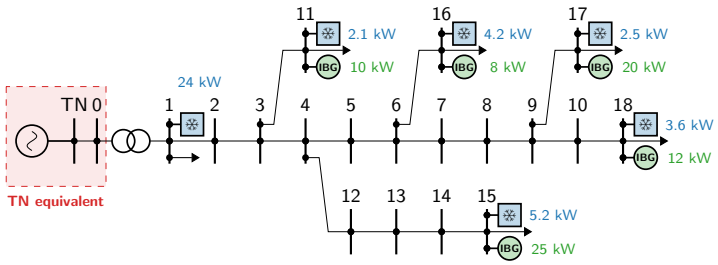

Fig. 8. Overview of the applied and adjusted CIGRE 18 Bus test case. Initial power consumption and generation of the distributed units is stated in the corresponding color next to the unit.

TABLE II
Protection and Support Parameters.

Common		ATL units		IBG units	
$df_{\max}$	±4 Hz/s	$f_{\min}$	49.5 Hz	$f_{\min}$	47 Hz
V_{pll}	0.8 p.u.	$f_{\max}$	55 Hz	$f_{\max}$	51.5 Hz
V_{int}	0.5 p.u.	$V_{\max}$	1.3 p.u.	$V_{\max}$	1.1 p.u.
$V_{\min}$	0.3 p.u.	V_1	0.9 p.u.	$k_1 = k_2$	4
V_{r}	0.9 p.u.	V_2	0.935 p.u.	$m = n$	0.2
T_1	0.3 s	$df^{\text{up}} = df^{\text{dn}}$	20	$df^{\text{up}} = df^{\text{dn}}$	20
T_2	1.5 s				
T_{int}	0.7 s				

To identify the contributions of the different unit types, the following four cases are examined:

- *All off*: protection and local support are disabled
- *IBG on*: IBG support and protection are enabled, while ATL support and protections are disabled
- *ATL on*: ATL support and protection are enabled, while IBG support and protections are disabled
- *All on*: support and protection from all units are enabled

For each of the cases, 200 simulations with randomized parameters as detailed in Sect. III are performed. Considering the results in [6] and the discussion in [18], the selected amount of simulations is sufficient to capture the average response.

For each of the scenarios the DN is subjected to two distinct TN faults: one over-frequency event with a loss of load of 0.2 MW and an under-frequency event with a load increase of 0.2 MW. Both load steps occur at the node the SM is connected to.

For each of the MC simulations, the power exchange at the TN/DN interface, i.e. the power flow across the transformer, and the grid frequency are captured. Furthermore, the maximum frequency deviation from nominal $|\Delta f^{\max}|$ and the maximum ROCOF $|df|^{\max}$ are evaluated. Unlike in the model of the protection, the ROCOF shown in the results is computed instantaneously without any delay. Thus, the units remain connected even if the displayed ROCOF exceeds the protection limit stated in Tab. II.

D. Results

The MC simulation results for the power exchange at the TN/DN interface (P_t, Q_t) for the strong grid, when subjected to an over-frequency event, are showcased in Fig. 9 for different protection and support settings. When no local support is provided, referring to the top plot in Fig. 9, the IBGs and ATLs draw constant power. During the initial transient, their outer control loops stabilize the power to the pre-fault value. The slight increase in steady-state consumption originates from the voltage sensitive loads. This increase in base load leads to more support from the DN and thus supports the TN frequency.

The cases in which only one group of devices provide support, i.e. the IGB only and ATL only cases, show similar behavior as seen in the second and third graph in Fig. 9. Right after the fault, the active power consumption of the DN drops mainly due to the

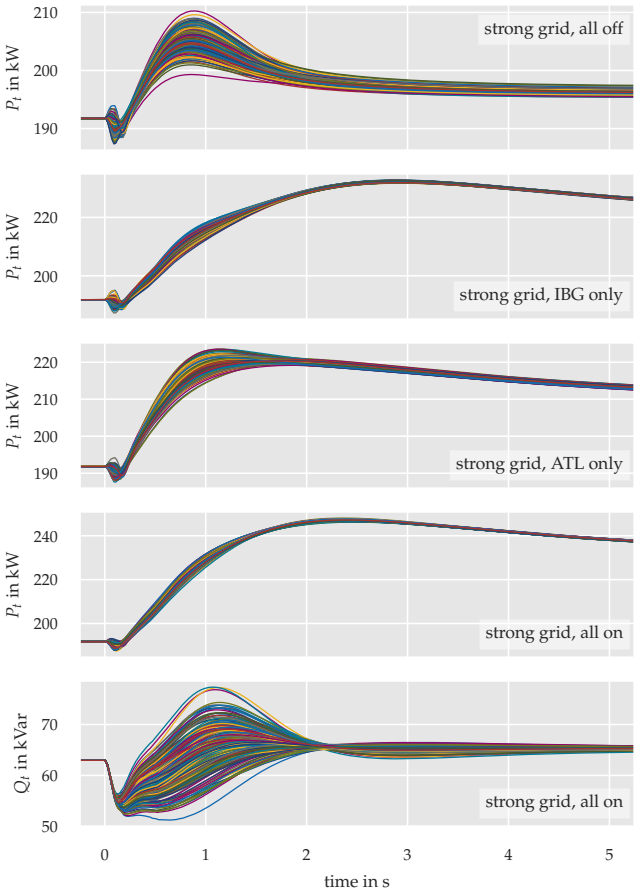

Fig. 9. Time-domain MC simulation results for the strong grid case when subjected to an over-frequency event.

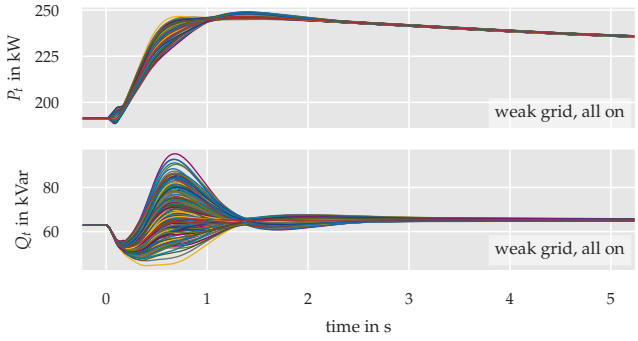

Fig. 10. Time-domain MC simulation results for the weak grid case when subjected to an over-frequency event with all support and protection activated.

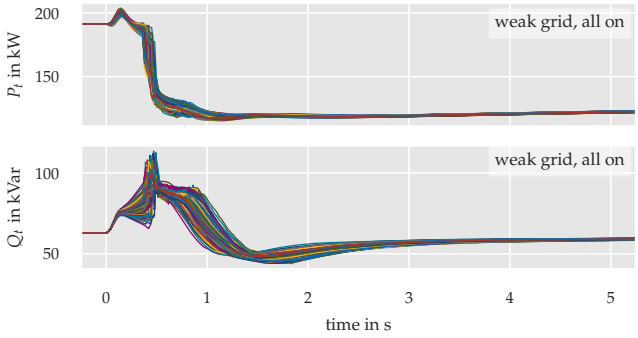

Fig. 11. Time-domain MC simulation results for the weak grid case when subjected to an under-frequency event with all support and protection activated.

voltage dip. Then, the droop controls detect a frequency mismatch and ensure the provision of local support. The variance throughout the MC simulations seems higher when only ATLs are active. At the same time, the loads supply a slightly faster reserve.

The smallest variance in active power exchange is achieved when all units provide support. In addition, the amplitude of the active power drawn from the TN is highest in this case. The result implies that the uncertainty of load and IBG parameters has little effect on the active power exchange when grid code parameters, such as the protection settings, are known accurately.

Unlike the active load, the reactive power varies significantly across the MC simulations. Since it behaves similarly for all test cases with the strong grid subjected to an over-frequency event, only one case is shown in Fig. 9. The consumption mainly stems from the base loads and their response to voltage deviations since all active components operate at one power factor.

Fig. 10 depicts the MC simulation results for the weak grid during an over-frequency event when all devices provide support. Compared to the strong grid scenario, the variance in active power increases, and the response speeds up. The latter is caused by the reduction in system inertia and faster frequency dynamics. In addition, the amplitude is slightly higher than for the strong grid case. The same holds for the reactive power exchange.

In Fig. 11 the weak grid is subjected to an under-frequency event with all local support activated. In contrast to the over-frequency event where continuous support could be provided, the ATL units switch off in this test case because their minimum frequency is undermined. However, the variance is still modest.

The effect of the variance in power exchange on TN frequency metrics is showcased in Fig. 12 for the strong and Fig. 13 for the weak grid scenarios. The frequency deviation is always highest without local support. As expected, the amplitude of frequency mismatch is higher when the TN is weak. Similarly, the variance of the frequency deviation is much higher for weaker TN systems.

While the activation of IBG support in the strong grid case reduces the median deviation by 100 mHz compared to the all off case, the change in the mean deviation is significantly less for weak grids. This results from the effect of grid strength on DN voltages. When the TN grid is weak, DN voltages change considerably more, such that local voltage support from IBGs might be required. Due to space limitations, no graph is shown, but voltages were observed in the simulation results. Note that ATLs with aggressive current controllers cause the outliers in the first two cases of the weak grid scenario.

When only IBGs supply reserve in the strong grid case, depicted by Fig. 12, the median frequency deviation is almost the same for the two frequency events. This originates from the parameterization of the units. Even though the frequency protection limits are asymmetric, their threshold is not reached for both disturbances and only a few devices hit interal limits during the under-frequency event, i.e. most IBGs are still able to supply continuous reserve during both frequency events. When the grid is weak as shown in Fig. 13, the difference in the median frequency deviation increases, as more IBGs saturate during the under-frequency event.

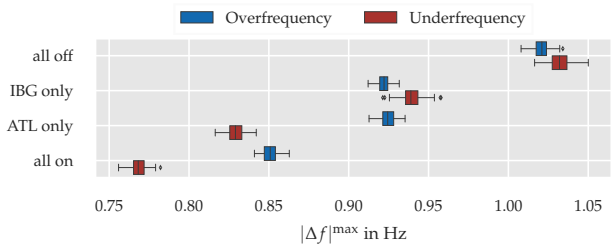

Fig. 12. Boxplot of the maximum frequency deviation in the strong grid scenario for all protection and support cases and both frequency events.

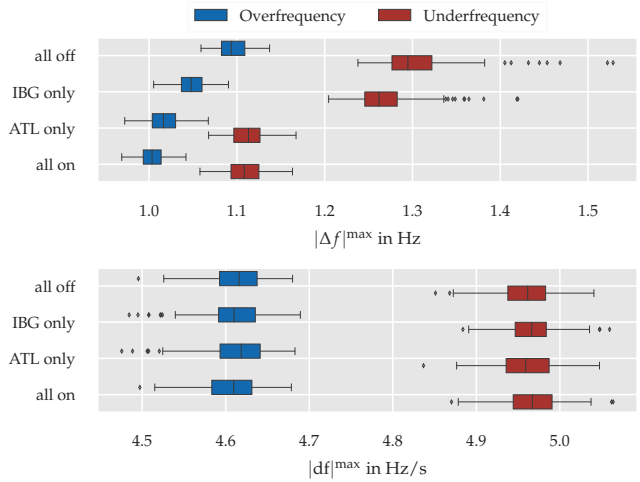

Fig. 13. Boxplot of the maximum frequency deviation and ROCOF in the weak grid scenario for all protection and support cases and both frequency events.

On the contrary, when only ATLs provide support in the strong grid case, the median frequency deviation for an under-frequency differs considerably from the deviation during an over-frequency event. This originates from the eminently asymmetric frequency protection limits of the ATLs, e.g. 49.5 Hz and 55 Hz. While ATLs remain connected during the over-frequency event, they switch off during the under-frequency. In the weak grid case, this difference in the median frequency deviation is lower because the support is saturated. Similar findings emerge when all units provide local support, highlighting the importance of considering all units during modeling.

Since the ROCOF's median is not much affected by the different support scenarios, it is only shown for the weak grid scenario. The MC simulations confirm previous findings on the limited effect of droop control on the maximum ROCOF levels.

Overall, the results indicate that careful consideration of unit models and their uncertainty is required, especially for modeling active DNs located in weak TN systems. In the case of the strong grid the variance is limited. However, this might change when protection and local support settings are not accurately known, i.e. when local units do not fully comply with grid codes.

V. Conclusion

This paper provides an extended model for ATL units by including local support and protection functions required for active demand-side units by modern grid codes. Furthermore, a MC time-domain simulation approach is suggested to study the uncertainty at TN/DN interfaces. While protection and support parameters are assumed accurate, the modeled uncertainty stems from the load and IBG parameters not outlined in grid codes. Finally, MC simulations for various scenarios are performed.

The results highlight the importance of carefully considering uncertainty, especially in stability studies of weak systems. While the variance of exchanged active power and the frequency deviation for strong grid scenarios are small and decrease with the amount of provided support, they considerably rise in weak TNs.

In addition, results indicate the significance of accurately modeling all grid supporting devices, including demand-side resources, for stability studies. Even for the strong grid case, the frequency deviation is notably affected when both ATLs and IBGs, and not only IBGs as is common in stability studies nowadays, are considered. However, the influence of local protection and support settings on the uncertainty remains to be studied. Future research should investigate which share of load units significantly affects TN states of interest and consider the uncertainty of the initial operating conditions, especially for the ATLs.

References

[1] H. Karbouj, Z. H. Rather, D. Flynn, and H. W. Qazi, "Non-synchronous fast frequency reserves in renewable energy integrated power systems: A critical review," *International Journal of Electrical Power & Energy Systems*, vol. 106, pp. 488–501, 2019.

[2] U. Markovic, O. Stanojev, P. Aristidou, E. Vrettos, D. Callaway, and G. Hug, "Understanding small-signal stability of low-inertia systems," *IEEE Trans. Power Syst.*, vol. 36, no. 5, pp. 3997–4017, 2021.

[3] J. Chen, M. Liu, and F. Milano, "Aggregated model of virtual power plants for transient frequency and voltage stability analysis," *IEEE Trans. Power Syst.*, vol. 36, no. 5, pp. 4366–4375, 2021.

[4] O. Stanojev, J. Rüssli-Kueh, U. Markovic, P. Aristidou, and G. Hug, "Primary frequency control provision by distributedenergy resources in active distribution networks," in *2021 IEEE Milan PowerTech*, 2021.

[5] G. Chaspierre, P. Panciatici, and T. Van Cutsem, "Modelling active distribution networks under uncertainty: Extracting parameter sets from randomized dynamic responses," in *2018 Power Systems Computation Conference (PSCC), Dublin*, 2018.

[6] G. Chaspierre, "Reduced-order modelling of active distribution networks for large-disturbance simulations," Ph.D. dissertation, Universite de Liege, Belgium, 2020.

[7] H. Hui, Y. Ding, and M. Zheng, "Equivalent Modeling of Inverter Air Conditioners for Providing Frequency Regulation Service," *IEEE Trans. Ind. Electron.*, vol. 66, no. 2, pp. 1413–1423, Feb. 2019.

[8] J. Vorwerk, U. Markovic, P. Aristidou, E. Vrettos, and G. Hug, "Modelling of variable-speed refrigeration for fast-frequency control in low-inertia systems," *IET Smart Grid*, vol. 3, no. 6, pp. 924–936, 2020.

[9] "IEEE Standard for Interconnection and Interoperability of Distributed Energy Resources with Associated Electric Power Systems Interfaces," Standard 1547-2018, 2018.

[10] "Establishing a network code on requirements for grid connection of generators," Commission regulation (EU) 2016/631, 04 2016.

[11] "Grid connection of energy systems via inverters - part 2: Inverter requirements," Standard New Zealand / Standards Australia, Tech. Rep. AS/NZs 477.2:2020, 2020.

[12] P. Kundur, *Power System Stability and Control*. McGraw-Hill, 1994.

[13] J. Vorwerk, U. Markovic, and G. Hug, "Fast demand response with variable speed thermal loads - towards universal modeling for stability assessment," in *2021 North American Power Symposium (NAPS)*, 2021.

[14] EPRI, "Simple Model Specification for Battery Energy Storage Systems ," WECC, Tech. Rep., 2015.

[15] EPRI, "Specification of the Second Generation Generic Models for Wind Turbine Generators ," WECC, Tech. Rep., 2013.

[16] E. Vrettos, C. Ziras, and G. Andersson, "Fast and reliable primary frequency reserves from refrigerators with decentralized stochastic control," *IEEE Trans. Power Syst.*, vol. 32, no. 4, pp. 2924–2941, Jul. 2017.

[17] Task force on turbine-governor modeling , "Dynamic Models for Turbine-Governors in Power System Studies ," IEEE, Tech. Rep., 01 2013.

[18] C. Mooney, *Monte Carlo Simulation*. SAGE Publications, 1997.

[19] CIGRE , "Benchmark Systems for Network Integration of Renewable and Distributed Energy Resources," CIGRE, Tech. Rep., 04 2014.

[20] BMWi, "Energieeffizienz in Zahlen: Entwicklungen und Trends in Deutschland 2019," BMWi, Tech. Rep., 08 2019.

[21] A. Petros, S. Lebeau, and T. Van Cutsem, "Power system dynamic simulations using a parallel two-level schur-complement decomposition," *IEEE Trans. Power Syst.*, vol. 31, no. 5, pp. 3984–3995, Sept 2016.